Cold-Spray Repair of Corroded Steel Bridge Girders via an Optimization-Driven Cyber-Physical Workflow and Robotic Deposition Architecture

Georgios Tzortzinis[a,*], Kaushik Abhyankar[a], Bruno Guilherme Christoff[a], Brian Schagen[b], A. John Hart[c], Simos Gerasimidis[b], Maik Gude[a]

[a] *Dresden University of Technology, Institute of Lightweight Engineering and Polymer Technology, Holbeinstraße 3, Dresden, Saxony 01037*
[b] *University of Massachusetts Amherst, Department of Civil and Environmental Engineering, 130 Natural Resources Road, Amherst, MA, 01003*
[c] *Massachusetts Institute of Technology, Department of Mechanical Engineering, 77 Massachusetts Avenue, Cambridge, MA, 02139*

Abstract

Corrosion-induced material loss in steel bridge poses persistent persistent challenges for inspection, load rating, and rehabilitation, often leading to conservative decisions and labor-intensive repair strategies. This paper presents a cyber-physical workflow for optimized repair design and a robotic cold-spray deposition architecture targeting corroded steel bridge girders. The framework integrates laser scanning, corrosion mapping, nonlinear finite element analysis, and gradient-based optimization to generate material-efficient cold-spray repair geometries tailored to the as-is condition of deteriorated members. Three-dimensional point cloud data are processed into a structured thickness field that captures localized corrosion while remaining computationally efficient for iterative optimization. Using this representation, spatially varying cold-spray deposition thickness fields are determined to maximize load-carrying capacity recovery while minimizing added material. Both Pareto-based and penalty-based optimization formulations are explored, enabling efficiency-driven trade-off analysis or direct targeting of prescribed capacity levels. The computational framework is validated against full-scale experimental testing of a naturally corroded steel girder, demonstrating close agreement between predicted and measured structural response. To connect optimized repair design with execution, a robotic cold-spray deposition architecture and a dedicated slicing strategy are introduced, together with a virtual environment for simulating deposition kinematics and process constraints. The proposed workflow establishes an integrated, data-driven pathway toward automated, performance-informed cold-spray repair of steel bridge infrastructure.

*Corresponding author
Email address: georgios.tzortzinis@tu-dresden.de (Georgios Tzortzinis)

Keywords: Cold spray, Additive manufacturing, Laser Scanning, Virtual twins, Finite Element Analysis

1. Introduction

Corrosion is a complex, multi-physics degradation process governed by electrochemical reactions, environmental exposure, and material heterogeneity, resulting in highly nonuniform and evolving patterns of material loss. In steel structural systems, this process manifests as spatially irregular section reduction that is strongly influenced by local geometry, detailing, and exposure conditions. For steel bridges, corrosion frequently localizes at beam ends, web-flange junctions, and other moisture-retaining regions. Even modest material loss can have disproportionate effects on stiffness, load path redistribution, and local or global stability phenomena [1, 2, 3, 4]. Experimental and numerical studies have shown that such localized deterioration can govern failure modes and residual capacity even when overall section loss appears limited [5, 6, 7]. Despite this inherent geometric and mechanical complexity, corrosion is commonly represented in engineering practice using simplified or idealized descriptions that inadequately capture its spatial variability. This disconnect between the physical manifestation of corrosion and its engineering representation propagates uncertainty throughout inspection, load rating, and repair decision-making, often leading to overly conservative assumptions and interventions.

Current repair practices for corroded steel girders are well established but remain costly and labor-intensive. Conventional rehabilitation typically involves localized reinforcement through welded steel plates [8] or bolted steel sections [9], requiring extensive surface preparation, skilled labor, and prolonged traffic disruptions. Alternative approaches, such as carbon fiber-reinforced polymers (CFRP), have demonstrated effectiveness in restoring capacity while reducing added weight [5, 10], but raise concerns related to durability, fire resistance, and long-term performance under harsh environmental exposure. Other strategies include welded stiffeners or studs embedded in grout or resin systems [11, 6], as well as partial or full encasement of deteriorated regions using ultrahigh-performance concrete (UHPC) [12]. UHPC-based repairs have shown promising mechanical performance through push-out testing [13, 14] and durability under accelerated electrochemical corrosion [15], with recent efforts moving toward field implementation [16]. Despite their effectiveness, these repair methods are typically solutions that apply uniform strengthening measures over large regions, offering limited adaptability to the highly localized and irregular nature of corrosion damage.

As a result, repairs are often conservative, material-intensive, and difficult to tailor to the actual structural demand, highlighting the need for more flexible, data-informed, and mechanically efficient rehabilitation strategies.

Additive manufacturing (AM) technologies open new opportunities for structural repair by enabling spatially resolved material placement that can be directly informed by mechanics, damage state, and performance objectives. From a structural standpoint, AM allows reinforcement to be distributed non-uniformly and applied only where it contributes meaningfully to stiffness recovery, load redistribution, or delay of local instability mechanisms, rather than relying on discrete or uniform strengthening measures. AM therefore enables the integration of structural analysis and optimization with fabrication, supporting material-efficient repair strategies.

Among AM approaches, wire arc additive manufacturing (WAAM) and related directed energy deposition (DED) processes have demonstrated scalability for large steel components and have been shown to produce structural steels with favorable mechanical performance and controlled microstructures [17, 18, 19]. However, the reliance of these processes on localized melting and solidification introduces significant thermal input, residual stresses, and metallurgical transformations that can complicate on-site repair. In contrast, cold-spray additive manufacturing (CSAM) has emerged as a particularly promising alternative for infrastructure repair due to its solid-state deposition mechanism, in which high-velocity particles plastically deform and bond to the substrate without bulk melting [20, 21, 22]. Bonding in cold spray is generally attributed to severe plastic deformation, adiabatic shear instability, and localized interfacial mixing, enabling strong adhesion while largely preserving the base-metal microstructure and minimizing thermal distortion [23, 24]. Cold spray has been explored for repairing damaged steel components and localized section loss [25], although its structural application at bridge-relevant scales remains an active area of research, with ongoing efforts needed to better characterize interface behavior, mechanical performance, and long-term durability under realistic loading and environmental conditions. In this context, cold spray may be a compelling platform for mechanically informed, data-driven repair strategies.

The potential effectiveness such repair strategies is inherently tied to the quality and resolution of inspection data. Traditional inspection practices for steel bridges rely heavily on visual assessment, isolated thickness measurements, and qualitative documentation, which fail to capture the spatial randomness and

severity of corrosion. In contrast, emerging sensing technologies such as 3D laser scanning, photogrammetry, and image-based reconstruction enable high-resolution mapping of surface geometry and deterioration patterns [26, 27, 28, 29]. These techniques have been successfully applied to damage detection [30, 31, 32] and quantitative assessment of corrosion in steel components [33, 4, 7]. Prior work by the authors has demonstrated that detailed corrosion morphology derived from 3D scans can be integrated directly into computational models for accurate capacity prediction of corroded steel girders [34]. Such data-rich representations provide the necessary geometric foundation for optimization-driven and additive repair strategies.

Building on these advances, this work presents a unified cyber–physical workflow tailored to cold-spray–based repair of corroded steel bridge girders, as schematically illustrated in Fig. 1. The framework integrates corrosion mapping by high-resolution laser-scanning with nonlinear finite element analysis and gradient-based optimization to determine spatially varying cold-spray deposition fields that efficiently restore structural capacity while minimizing added material. To enable translation from optimized repair design to execution, the study introduces a robotic cold-spray deposition architecture and an associated slicing and path-planning strategy that convert thickness fields into machine-interpretable trajectories. A virtual twin of the deposition system is developed to simulate kinematics, stand-off control, and process sequencing. Material behavior used in the computational framework is informed by experimental testing of cold-spray–repaired steel specimens, while the predicted structural response is validated against full-scale testing of a naturally corroded girder. Collectively, the proposed methodology establishes an end-to-end, data-driven pathway, addressing key limitations of conventional repair practice and supporting repeatable, performance-informed rehabilitation of steel bridge infrastructure.

2. Scan-to-Model Corrosion Mapping

Building on scan-to-FEM workflows previously developed and experimentally validated by the authors for residual capacity prediction of corroded steel girders [34], the present work refines and systematizes the corrosion representation to support gradient-based topology optimization. The key requirement for the subsequent design stage is a corrosion description that is (i) accurate to the measured deterioration, (ii) computationally efficient for repeated finite element analyses, and (iii) expressed in a parameterized form suitable for automated material-volume estimation, sensitivity analysis, and downstream fabrication

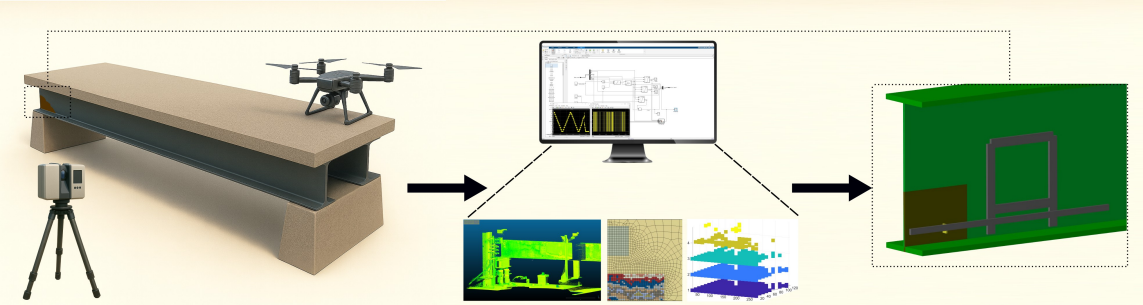

Figure 1: Overview of the proposed cyber-physical workflow for cold-spray repair of corroded steel bridge girders. High-resolution point cloud data are processed to derive spatially resolved web-thickness fields, which inform nonlinear finite element analysis and gradient-based optimization. The resulting optimized deposition fields are translated into executable trajectories for automated cold-spray repair.

planning. To meet these requirements, the contour-based thickness representation in [34] is reformulated into a structured, block-wise thickness field.

Point cloud data in this study were acquired on a 24CB120 beam under laboratory conditions using a RIEGL VZ-2000 LiDAR scanner [35]. The proposed algorithmic framework is not tied to specific hardware and can be applied to other terrestrial, portable, or drone-mounted scanners, provided that the resulting point clouds satisfy the accuracy and precision needed to capture local section-loss features relevant to capacity and stability. The processing pipeline from raw point cloud to thickness field is fully scripted, enabling deployment within automated inspection-to-repair workflows.

2.1. Converting scan data to an optimization-ready thickness field

Previous research by the authors demonstrated that scan-derived contour maps can represent corrosion profiles with high fidelity and support accurate computational prediction of residual capacity [34]. While well-suited for detailed assessment and one-off analyses, purely contour-based geometries are less compatible with automated, iterative optimization frameworks. Specifically, (i) variable element sizes and irregular partitions complicate automated estimation of deposited material volume, (ii) the large number of partitions required to represent complex corrosion surfaces increases model generation time, and (iii) the resulting model complexity limits scalability for repeated analyses.

To address these limitations, a structured grid–based representation is introduced to describe the remaining web thickness field in a form suitable for optimization. Unlike the contour-based description shown in

Fig. 2a, which preserves the full geometric fidelity of the corrosion morphology through irregular, free-form boundaries, the structured grid representation in Fig. 2b discretizes the same corrosion field into a finite number of rectangular blocks with uniform in-plane dimensions. Each block is assigned a single representative thickness value, transforming the continuous corrosion morphology into a piecewise-constant field that is computationally tractable and directly compatible with optimization algorithms.

Prior experimental and numerical investigations by the authors determined that the lower part of the web governs the load-carrying capacity and failure behavior of corroded girder ends [1, 2]. Accordingly, only this region is discretized using the structured grid, while the remainder of the web is assumed to retain uniform nominal thickness. This targeted discretization significantly reduces model size and computational cost while preserving the structural fidelity required for capacity prediction. The validity of this representation is assessed through comparison with full-scale experimental results reported previously by the authors [34].

To examine sensitivity to grid resolution, the corrosion domain (19 cm $\times$ 40.6 cm) is discretized using two configurations: 576 blocks (18 $\times$ 32) and 2,368 blocks (37 $\times$ 64). The remaining thickness is quantized into 10 and 12 discrete thickness levels for the coarse and fine grids, respectively (Fig. 2c–d). This discretized field constitutes a compact, machine-readable state variable that can be directly coupled with topology optimization and fabrication path planning.

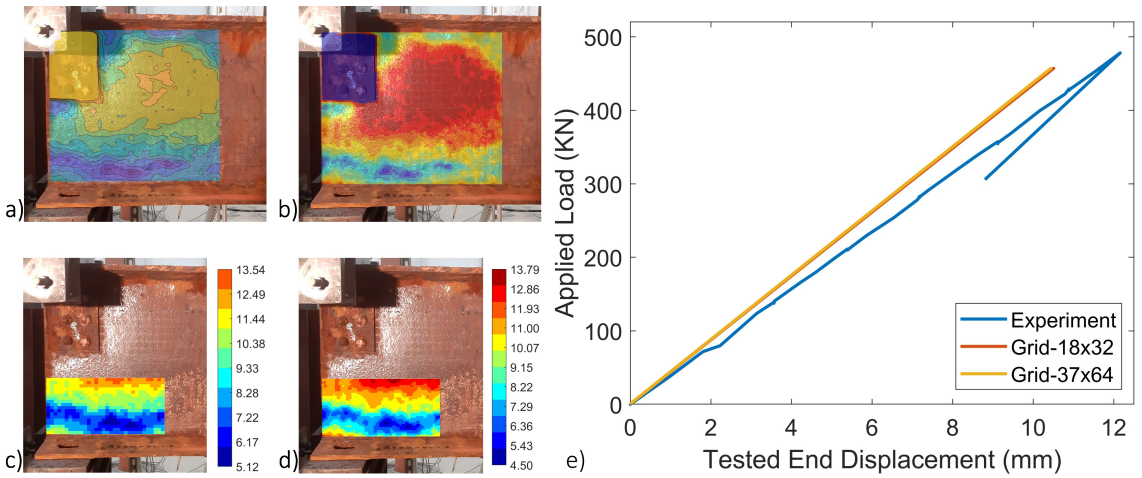

Figure 2: Corrosion mapping and experimental validation for a 24CB120 beam end. (a) Remaining web thickness represented using contour-based interpolation of 3D scan data. (b) Structured grid representation of the same corrosion profile. For computational efficiency, only the governing lower portion of the web is considered in the capacity evaluation, with a (c) coarse and (d) dense mesh being evaluated. (e) Comparison of experimental and numerical load–displacement responses for coarse and fine grid resolutions.

2.2. Experimental benchmark and numerical validation

A full-scale destructive test previously performed by the authors on a 24CB120 beam with the corrosion pattern shown in Fig. 2 is used as the benchmark for validating the proposed corrosion representation [34]. For completeness, the experimental configuration is illustrated in Fig. 3b. The specimen is simply supported, and the load is applied upward using two hydraulic jacks positioned beneath the tested end. A crossbeam anchored to the strong floor is placed 1.2 m from the tested end to restrain vertical movement. Out-of-plane displacement of the top flange is restricted using lateral braces to suppress lateral–torsional buckling. The reaction force at the tested end is measured using three load cells (1x445 kN, 2x890 kN by Omega), and the corresponding deflection is recorded with a cable extension position transducer (Calesco PT101). The exact technical specifications of the implemented equipment are given in [34, 1].

For validation and for automated integration into the optimization framework, the scan-derived grid representation is embedded into a three-dimensional finite element model using Abaqus. The algorithmic pipeline developed in [34] is adapted to use the structured grid in place of contour maps. A MATLAB script extracts grid-line coordinates and generates the thickness map corresponding to Fig. 2b–d, while a Python script is used to partition the web surface data and assigns the associated thickness values automatically to the finite element model.

The girder is modeled using four-node linear S4R shell elements with a midsurface approximation, consistent with the slender web and flange geometry [34, 3, 2]. A mesh size up to 6.5 cm is used away from the corroded end, while one element is assigned to each rectangular block within the corrosion domain to preserve the imposed thickness field. Boundary conditions, loading, and material properties are defined to replicate the experimental configuration, with mechanical properties obtained from tensile testing of coupons extracted from the web and flanges, as reported in [34].

Figure 2d compares the experimentally measured load–displacement response to finite element predictions obtained using the two grid resolutions. The ultimate capacity is predicted as 456.7 kN and 457.0 kN for the coarse and fine grids, respectively, in close agreement with the experimentally measured capacity of 478 kN (discrepancy of -4.4%). The similarity of the coarse- and fine-grid predictions indicates that the coarse grid retains the governing corrosion features relevant to capacity and stability, while offering substantially improved computational efficiency. Accordingly, the coarse-grid representation is adopted in

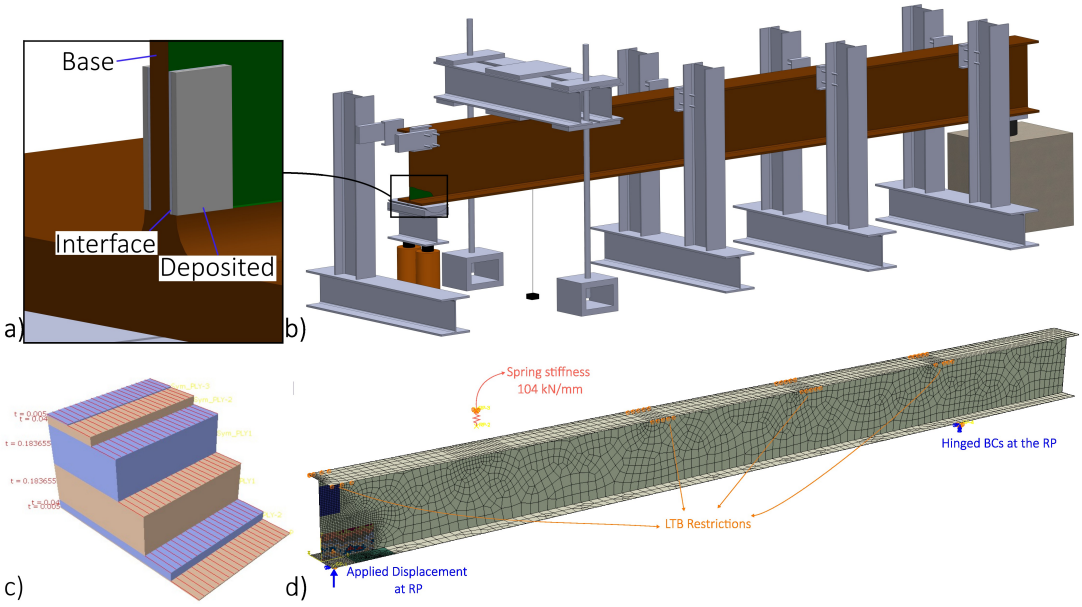

Figure 3: Repair strategy, experimental setup, and finite element model. Schematic of (a) the repair strategy where the added material is shown as a simplified rectangle of constant thickness and (b) the full-scale experimental test setup, showing the simply supported girder, applied vertical loading at the corroded end, and restraint provided by the strong floor. (c) Finite element representation of the three-layer composite shell model, including the base, interface, and additive layers applied symmetrically on both web surfaces. (d) Boundary and loading conditions used in the numerical simulations for the optimization studies.

the subsequent optimization studies.

3. Computational Optimization Framework for Additive Repair Design

Cold-spray additive manufacturing enables the controlled deposition of metallic particles to form a dense, monolithic layer on a steel substrate, allowing corrosion-induced material loss to be rebuilt in a spatially resolved manner. From a structural mechanics perspective, this capability creates a direct pathway for restoring load-carrying capacity toward the pre-corroded (intact) condition of steel bridge components, rather than relying on conservative, uniform strengthening measures. By selectively adding material where stiffness, load-path continuity, or local stability have been compromised, cold spray repairs can recover structural performance while minimizing unnecessary intervention. The free-form nature of additive deposition enables reinforcement layouts that are tailored to the underlying mechanics of deterioration.This design freedom opens the door to optimization-driven repair strategies, in which material placement and thickness distribution are

determined systematically to maximize capacity recovery and efficiency. To exploit this potential in a rigorous and automated manner, an optimization-based computational framework is formulated to determine where and how much material should be deposited to restore structural performance with minimal added material. Within the broader cyber–physical workflow introduced in this paper, the optimization module serves as the decision-making engine that translates scan-derived deterioration data into executable, material-efficient cold-spray repair designs.

The optimization problem seeks to determine the additional thickness field

$$\mathbf{t} = [t_1, t_2, \ldots, t_N]^\top, \tag{1}$$

applied symmetrically on both sides of the corroded web. Owing to the structured grid representation, each block i within the optimization domain has an identical in-plane area A, resulting in a fixed design space with a direct one-to-one correspondence between grid blocks and design variables. Consistent with the mid-surface shell formulation adopted in the finite element model, the geometry and loading are assumed to be symmetric about the web mid-plane, which reflects both the physical repair strategy and facilitates automated fabrication.

When a grid block is reinforced through cold-spray deposition, the repaired region is represented using a three-layer composite section (Fig. 3a), defined as:

i) **Base material layer**, representing the as-scanned remaining web thickness.

ii) **Interface layer**, a 1 mm transition zone with material properties representative of the bond region between the base metal and the deposited material, applied symmetrically on both sides.

iii) **Additive layer**, corresponding to the deposited cold-spray material and defined by the optimization variables t_i, applied symmetrically on both sides.

This layered representation provides a physically informed yet computationally tractable description of the repaired cross-section, allowing the mechanical contribution of the deposited material and the interface to be explicitly captured within the optimization loop.

To inform the layerwise properties to be incorporated in the model, mechanical tests were conducted on

reference specimens and specimens with cold spray deposits. Tests followed ASTM E9 using an Instron 5569 frame at a quasi-static nominal strain rate of 2×10^{-4} s^{-1}. A non-contact AVE2 laser extensometer, with a displacement resolution of 0.5 μm, was used to track axial strains, ε, via fiducial dots placed on opposing specimen faces to minimize grip compliance effects. Three specimen families were tested: (i) pure A36 pillars, (ii) pure cold-spray pillars (SS0X), and (iii) composite pillars comprising cold-spray material deposited on A36 with equivalent thickness. This test matrix enabled direct comparison of the σ–ε response across the different material systems.

The stress–strain curves shown in Fig. 4 distinguish the mechanical responses of pure A36 (black), composite A36–SS0X (blue), and pure SS0X (orange) pillars fabricated using SS08 powder. Markers indicate the yield stress, σ_y (rectangles), and the ultimate stress, σ_u (triangles). The A36 response exhibits the expected initial linear elastic regime up to σ_y, followed by stable plastic flow with pronounced strain hardening over a broad strain range (plotted up to 20% strain). For A36, the measured $\sigma_y = 313 \pm 12$ MPa and elastic modulus $E = 211 \pm 13$ GPa establish the baseline stiffness and strength against which the composite response is evaluated.

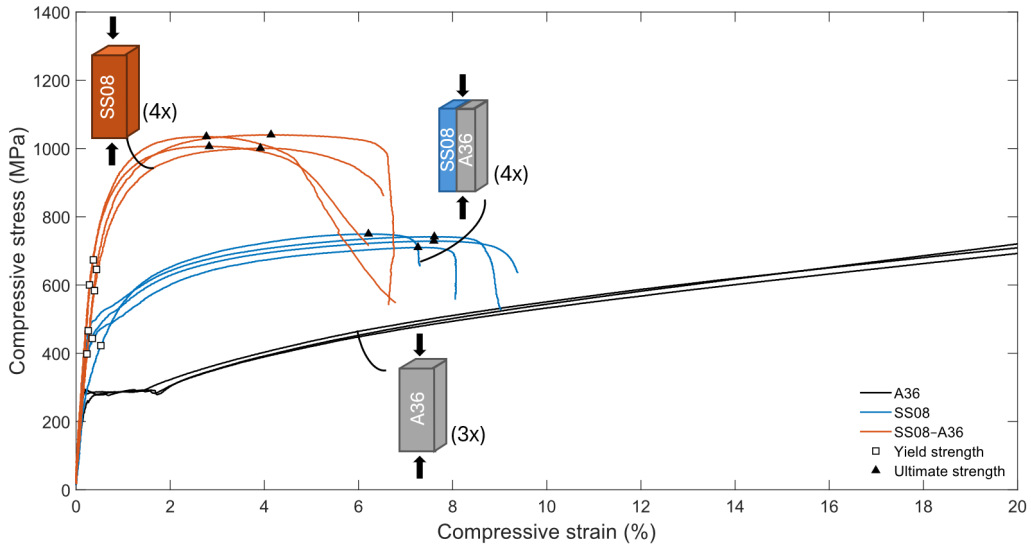

Figure 4: Stress–strain response of pillar specimens under uniaxial compression: (i) pure A36 specimens (black), (ii) composite SS0X–A36 specimens (blue), and (iii) pure SS0X specimens (orange).

Two complementary optimization strategies are investigated to address distinct repair design objectives

commonly encountered in bridge engineering practice and to support automated, repeatable decision-making. The first strategy employs a Pareto-based formulation to explicitly quantify the trade-off between added material volume and recovered structural capacity. This formulation enables systematic exploration of multiple admissible repair solutions and quantifies how local material deposition influences global performance. Such information is particularly valuable during preliminary assessment and option screening, where agencies often seek to understand efficiency trends, diminishing returns, and the structural consequences of alternative intervention levels before committing to a specific repair strategy.

The second strategy adopts a penalty-based formulation that targets restoration to a prescribed capacity level consistent with load-rating and serviceability objectives defined in AASHTO and MassDOT bridge evaluation procedures. In this case, the optimization enforces a direct performance requirement, such as recovery of the nominal pre-corrosion capacity, while minimizing the amount of deposited material. This approach mirrors current practice in which repairs are designed to meet explicit capacity thresholds, but does so within an automated, mechanics-based framework that replaces manual sizing and conservative assumptions with data-driven thickness allocation. Together, the two formulations enable both exploratory and target-driven repair design within a unified computational workflow, demonstrating how cold-spray additive manufacturing can be systematically integrated into automated bridge assessment and rehabilitation processes.

3.1. Pareto-Based Multi-Objective Optimization

The total added material volume and the corresponding gain in load-carrying capacity are defined as

$$V(\mathbf{t}) = 2\sum_{i=1}^{N} A\, t_i, \qquad L(\mathbf{t}) = \mathrm{Cap}(\mathbf{t}) - \mathrm{Cap}(0), \tag{2}$$

where $\mathrm{Cap}(\mathbf{t})$ denotes the global structural capacity associated with a reinforcement field $\mathbf{t}$, defined as the peak reaction force in the nonlinear load–displacement response of the finite element model. The factor of two accounts for symmetric deposition on both sides of the web. Based on these definitions, the optimization objective function is expressed as

$$\Phi(\mathbf{t}) = a\,\frac{V(\mathbf{t})}{V_{\mathrm{scale}}} - (1-a)\,\frac{L(\mathbf{t})}{L_{\mathrm{scale}}}, \qquad a \in [0,1], \tag{3}$$

where V_{scale} and L_{scale} are normalization factors chosen such that both terms have comparable magnitude. The weighting parameter $a \in [0, 1]$ controls the relative importance between material efficiency and structural performance. A value of $a = 1$ drives the optimization toward minimum added volume, whereas $a = 0$ emphasizes maximum capacity recovery. Intermediate values generate the Pareto front, capturing the trade-off between competing objectives.

The optimization follows a steepest descent scheme, where the descent direction is given by

$$\mathbf{d}_k = -\nabla\Phi(\mathbf{t}_k), \tag{4}$$

and the design variables are updated according to

$$\mathbf{t}_{k+1} = (\mathbf{t}_k + \eta\mathbf{d}_k)\,, \tag{5}$$

with η denoting the step size, taken as a constant value of 0.6. This choice was found to be adequate given the computational cost of nonlinear finite element evaluations and the numerical noise associated with finite-difference sensitivity calculations. The use of a small, fixed step size ensures stable descent without the need for line-search procedures.

The total gradient of the objective function is given by

$$\nabla\Phi(\mathbf{t}) = \frac{a}{V_{\text{scale}}}\nabla V(\mathbf{t}) - \frac{(1-a)}{L_{\text{scale}}}\nabla L(\mathbf{t}), \tag{6}$$

with

$$\nabla V(\mathbf{t}) = 2A, \qquad \nabla L(\mathbf{t}) = \left[\frac{\partial \text{Cap}(\mathbf{t})}{\partial t_1}, \ldots, \frac{\partial \text{Cap}(\mathbf{t})}{\partial t_N}\right]^\top. \tag{7}$$

The capacity sensitivities are approximated using forward finite differences,

$$\frac{\partial \text{Cap}(\mathbf{t})}{\partial t_i} \approx \frac{\text{Cap}(\mathbf{t} + \Delta t_{\text{side}}) - \text{Cap}(\mathbf{t})}{\Delta t_{\text{side}}}, \qquad i = 1, \ldots, N, \tag{8}$$

where Δt_{side} denotes the calibrated thickness increment applied symmetrically on both sides of the web. Manufacturing and physical feasibility are enforced through the constraints

$$0.25\ \text{mm} \le t_i \le 0.5\, t_{\text{web}}, \quad i = 1, \ldots, N. \tag{9}$$

The iterative process is terminated when both

$$\|\mathbf{t}_{k+1} - \mathbf{t}_k\| < \varepsilon_t, \qquad \|\nabla\Phi(\mathbf{t}_k)\| < \varepsilon_g, \tag{10}$$

are satisfied, with $\varepsilon_t = 0.006$ and $\varepsilon_g = 0.02$.

3.2. Penalty-Based Optimization for Target Capacity Recovery

In bridge rehabilitation applications, repairs are often designed to restore the structure to a prescribed target capacity associated with a specific load rating. To reflect this objective, a penalty-based optimization problem is formulated to achieve a target capacity L_{goal} while minimizing the added material volume.

The penalized objective function is defined as

$$\min_{\mathbf{t}} \ \Phi_{\text{pen}}(\mathbf{t}) = V(\mathbf{t}) + \mu \left(L_{\text{goal}} - L(\mathbf{t})\right)^2, \qquad V(\mathbf{t}) = 2\sum_{i=1}^{N} A\, t_i, \tag{11}$$

where μ is the penalty parameter controlling the relative emphasis placed on meeting the prescribed capacity target L_{goal}.

The total gradient of the penalized objective function is expressed as

$$\nabla\Phi_{\text{pen}}(\mathbf{t}) = 2A - 2\mu\big(L_{\text{goal}} - L(\mathbf{t})\big)\, \nabla L(\mathbf{t}), \tag{12}$$

where the sensitivity of the recovered capacity with respect to the per-side thickness variable t_i is approximated by

$$\frac{\partial L}{\partial t_i} \approx \frac{L(\mathbf{t} + \Delta t_{\text{side}}) - L(\mathbf{t})}{\Delta t_{\text{side}}}, \qquad i = 1, \ldots, N. \tag{13}$$

Here, Δt_{side} denotes the predetermined thickness increment applied symmetrically on both sides of the web.

The optimization proceeds via a projected gradient descent scheme,

$$\mathbf{d}_k = -\nabla\Phi_{\text{pen}}(\mathbf{t}_k), \qquad \mathbf{t}_{k+1} = (\mathbf{t}_k + \eta_k \mathbf{d}_k)\,, \tag{14}$$

where η_k is the step size, initially set to 0.2 and subsequently adapted based on observed numerical fluctuations.

Convergence is achieved when both the change in the design variables and the gradient norm satisfy

$$\|\mathbf{t}_{k+1} - \mathbf{t}_k\| < \varepsilon_t, \qquad \|\nabla\Phi_{\text{pen}}(\mathbf{t}_k)\| < \varepsilon_g. \tag{15}$$

Manufacturing and physical feasibility constraints identical to those employed in the Pareto-based formulation are applied. Specifically, the per-side deposited thickness at each grid block is constrained to remain within bounds that reflect both cold-spray process limitations and structural realism. A lower bound of 0.25 mm is imposed to represent the minimum reliably achievable deposition thickness per side, below which stable layer formation and repeatable material properties cannot be guaranteed. An upper bound of $0.5\,t_{\text{web}}$ is enforced to prevent excessive local thickening that could introduce unrealistic stiffness gradients, numerical instability, or impractical repair geometries relative to the remaining web thickness.

3.3. Automated Optimization Workflow and Model Updating

The optimization framework is implemented through an iterative finite element analysis workflow, as illustrated in Fig. 5. Starting from the corroded geometry, the procedure updates the thickness field $\mathbf{t}$ until convergence of both the objective function and the design variables is achieved.

At each iteration k, a set of modified finite element models ("delta files") is automatically generated. Each delta file corresponds to a predetermined thickness increment Δt of 2 mm applied symmetrically to both sides of a single element within the optimization domain. These delta files represent localized perturbations of the thickness field and can be interpreted as incremental candidate repair actions applied to individual grid blocks. If a block has not been previously repaired, an interface layer is introduced symmetrically; otherwise, the thickness increment Δt is applied on top of the existing repair layer.

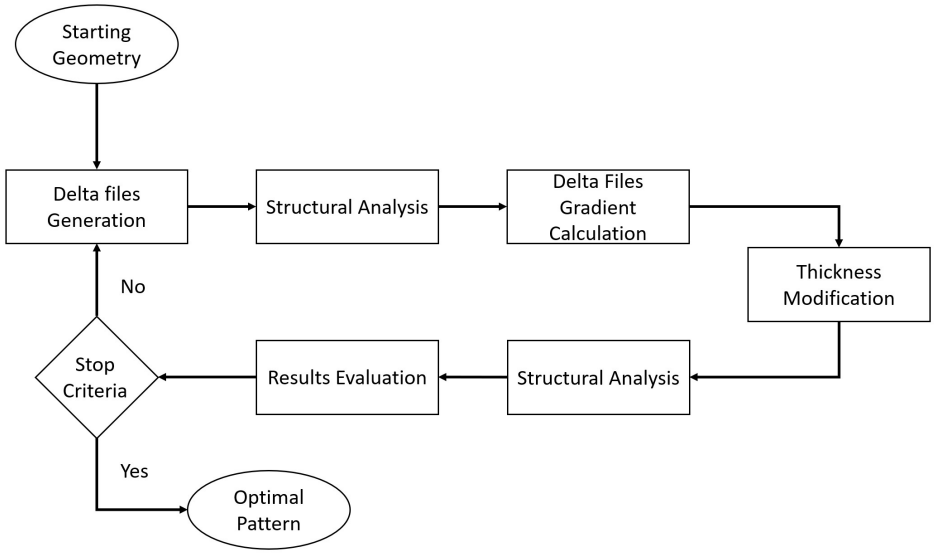

Figure 5: Flowchart of the gradient-based optimization algorithm. For each element, the effect of a predefined local thickness increase is evaluated by finite element analysis. The corresponding gradients are used to iteratively update the thickness field until convergence to the optimal repair pattern.

Each modified model is solved to evaluate the structural capacity, defined as the peak reaction force developed at the bearing of the corroded end. To enable efficient batch processing, the corresponding reaction forces are extracted automatically from the Abaqus output (.dat) files using the algorithmic framework.

Once the batch computation of reaction forces for all perturbations is completed, the element-wise sensitivities of the objective function are evaluated. The thickness distribution is then updated according to the gradient descent rules defined in Eqs. (5) and (14), followed by enforcement of the previously defined bound constraints

$$0.25\ \text{mm} \leq t_i \leq 0.5\, t_{\text{web}}. \tag{16}$$

The updated geometry is reanalyzed and the convergence criteria are checked. If convergence is not satisfied, the procedure advances to the next iteration; otherwise, the optimization terminates and the final repair pattern is obtained.

3.4. Finite Element Modeling of Repaired Beam Sections

The finite element model described previously is extended to incorporate the additional layers introduced in the repaired regions. This is achieved through symmetric composite shell section definitions in Abaqus, where each layer in the stacking sequence is specified by its thickness and corresponding material properties (Fig. 3c). The base, interface, and additive layers are assigned the experimentally derived constitutive models shown in Fig. 4b.

To reduce computational cost while retaining the governing structural response, the boundary and loading conditions are slightly simplified relative to the validation model described in [34]. Specifically, the self-weight of the girder and the weight of the crossbeam present in the experimental setup are omitted. The applied boundary and loading conditions used in the optimization analyses are shown in Fig. 3d.

These simplifications, combined with the structured grid representation of corrosion, result in a substantial reduction in computational effort. For the same hardware configuration and number of processors, the required analysis time is reduced from approximately 25 minutes for the contour-based model (Fig. 2a) to approximately 90 seconds for the grid-based representation applied to the lower portion of the web (Fig. 2c). This reduction in runtime is critical for enabling repeated nonlinear analyses within the iterative optimization procedure.

4. Optimization Results and Repair Design Outcomes

While the preceding sections establish the computational framework used to derive optimized cold-spray repair geometries, the practical value of the proposed methodology lies in the structural behavior and efficiency of the resulting repair patterns. This section therefore focuses on the outcomes of the optimization process, examining how spatially varying thickness fields influence load-carrying capacity recovery, material efficiency, and governing failure mechanisms in a corroded steel girder. Results are presented for both Pareto-based and target-capacity formulations, allowing direct comparison between trade-off–driven and performance-driven repair strategies. Emphasis is placed on interpreting the resulting deposition patterns in terms of structural mechanics, load-path modification, and their relevance to bridge load-rating and rehabilitation decisions.

4.1. Pareto-Optimal Repair Patterns and Trade-Offs

Next the Pareto front optimization technique is applied to the corroded beam shown in Fig. 2, using the optimization domain indicated by the black rectangle in Fig. 6c. The size of this domain is consistent with the area requirements used for evaluating the residual capacity of corroded beams in the MassDOT Bridge Manual [36] and with previous studies by the authors [37]. Fig. 6e illustrates the application of a thickness increment Δt to an individual grid element for gradient evaluation, as described in Section 3.3.

Figure 6 summarizes the resulting deposition patterns, along with the corresponding capacities and efficiencies obtained for values of α ranging from 0.0 to 0.8. Results for $\alpha > 0.8$ are omitted, as the thickness distribution remains unchanged relative to the unrepaired geometry. For $\alpha < 0.2$, examination of the finite element model results indicates that the failure mode is governed by yielding at the crossbeam location, away from the corroded end. This behavior is reflected in Fig. 6a–b, where the beam capacity converges on the left side of each diagram and the additional load sustained due to the repair approaches zero for $\alpha = 0.8$ in Fig. 6b.

In Fig. 6a, the dashed blue line denotes the nominal capacity of an intact beam. Although solutions with $\alpha < 0.4$ exceed this baseline value, the most efficient repairs, defined as the ratio of recovered capacity to deposited material volume, occur for higher α values, where the optimization emphasizes minimizing material use. For example, increasing the deposited volume by 45 cm^3 when moving from $\alpha = 0.3$ to $\alpha = 0.2$ yields only 26.9 kN of additional capacity, whereas adding just 25 cm^3 at $\alpha = 0.7$ results in a significantly larger increase of 189 kN.

The morphology of the corresponding cold spray deposition patterns is depicted in Fig. 6d, f, and h, showing respectively the deposited thickness, the total thickness, and the amount exceeding the nominal web thickness. As expected, the deposited volume increases progressively as α decreases. Notably, the solutions corresponding to $\alpha = 0.4$, 0.6, and 0.7 share a consistent structural layout characterized by two prominent vertical reinforcement zones positioned near the beginning and midpoint of the optimization region, and extend along the height of the optimization domain. These zones function similarly to added stiffeners and contribute substantially to the recovered capacity. The configuration corresponding to $\alpha = 0.6$ is shown in detail in Fig. 6g.

In contrast, the reinforcement patterns obtained for $\alpha = 0.3$ and $\alpha = 0.5$ follow a different strengthening

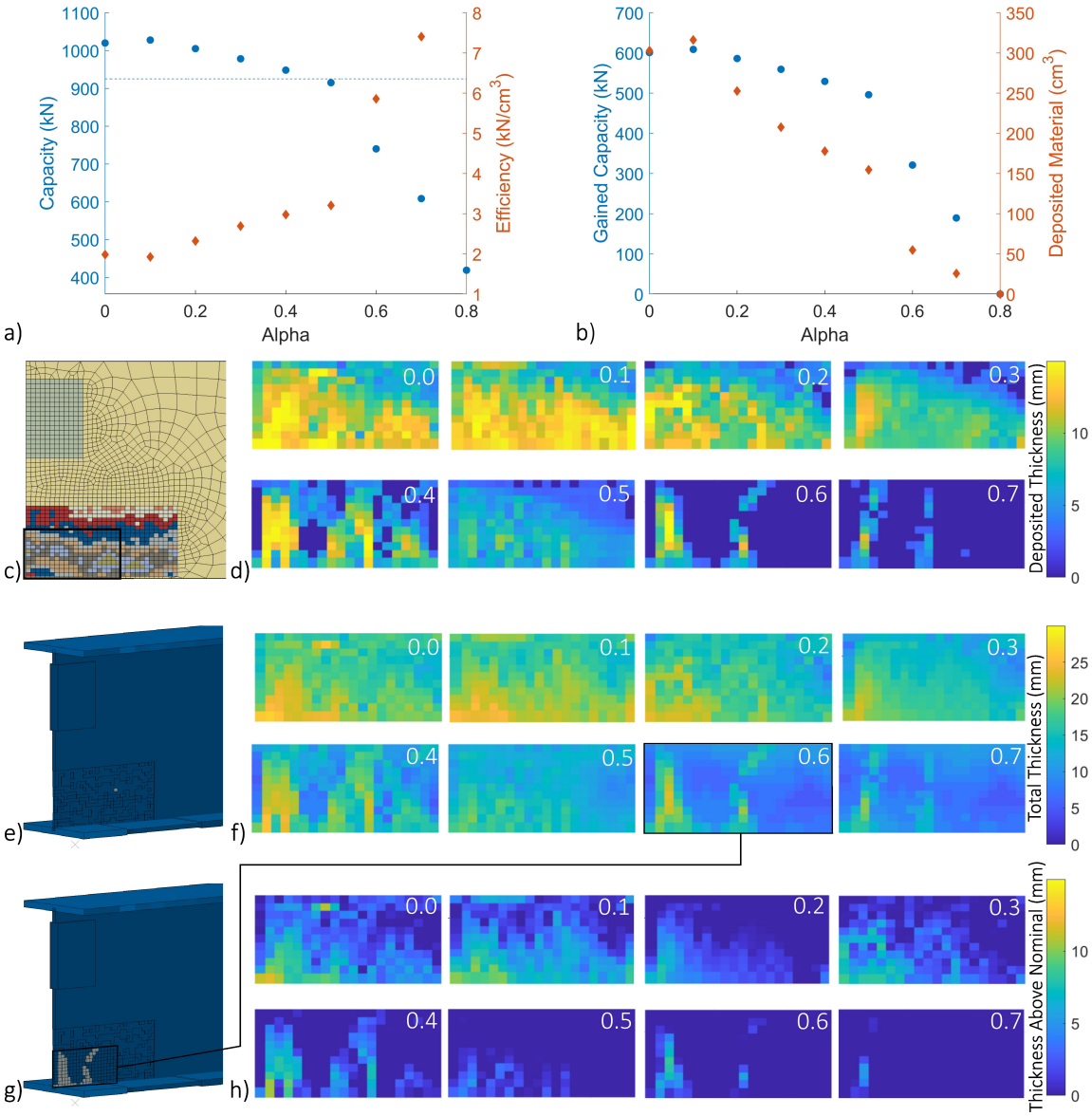

Figure 6: Results of the Pareto formulation for optimization of deposited reinforcement thickness. (a) Girder capacity versus efficiency and (b) recovered capacity versus deposited material for various α values. (c) Optimization domain indicated by the black box. (d) Resulting deposition thickness fields and total deposited thickness along both sides, (f) resulting thickness distributions, and (h) regions where the thickness exceeds the nominal web value within the prescribed domain (per side). (e) In the gradient-descent optimization scheme, each element in the optimization space is assigned a thickness increment Δt, and its influence on the overall capacity is evaluated. (g) Finite element model corresponding to the optimal solution for $\alpha = 0.6$.

strategy, distributing material more uniformly across a larger portion of the optimization domain. This distinction is particularly evident in Fig. 6h, where these solutions exceed the nominal web thickness over a noticeably greater area compared to the other α values.

The stopping criteria defined in Section 3.1 were intentionally selected to avoid overly restrictive convergence requirements, allowing a consistent optimization framework across all values of α. For each case, a sufficiently large number of iterations was performed to generate multiple admissible solutions. The final solution for each α was selected as the one yielding the minimum value of the objective function among all candidates. Figure 7 presents the evolution of capacity and deposited material, the gradient norm, and the objective function value for the representative case of $\alpha = 0.3$. These results confirm stable convergence of the optimization procedure.

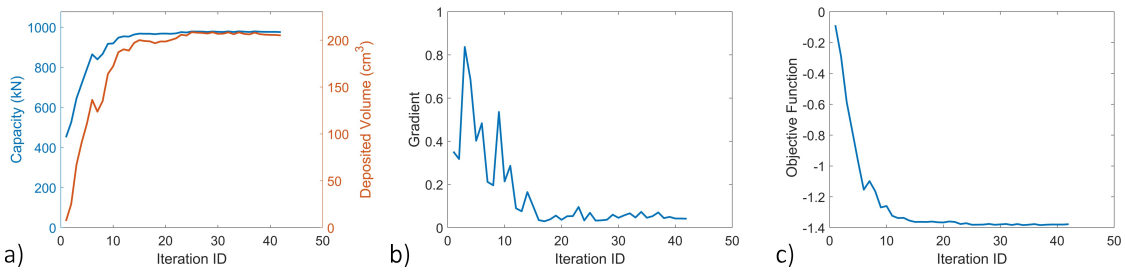

Figure 7: Convergence behavior of Pareto front optimization technique for $\alpha = 0.3$. a) Evolution of capacity and deposited material per iteration, b) gradient norm at the end of each iteration, and c) objective function value.

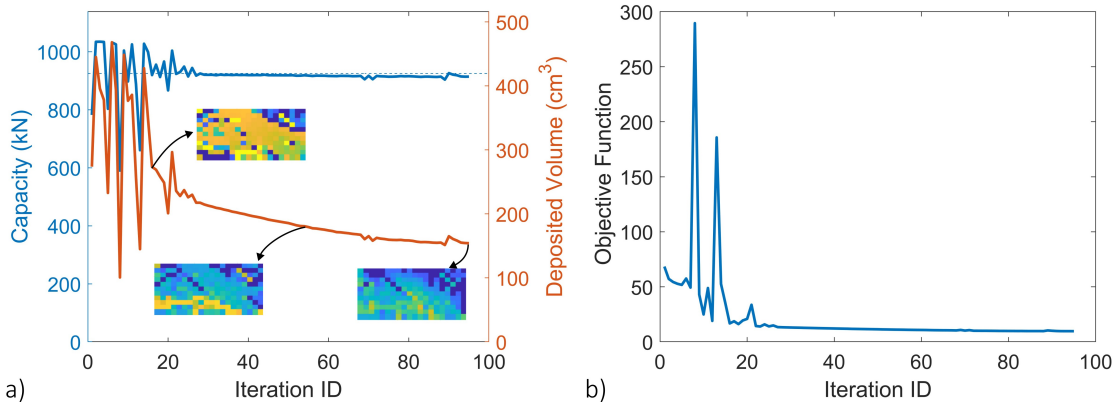

Figure 8: Penalty-based optimization results for complete capacity restoration. a) Iteration-by-iteration evolution of capacity, material deposition and three indicative repair scenarios, and b) objective function convergence.

4.2. Target-Capacity Repair Design Using Penalty Optimization

Repair of the same corroded beam end is next modeled using the penalty-based formulation introduced in Section 3.2. In this case, the optimization is tasked with restoring the nominal capacity of the intact section, defined as $L_{\text{goal}} = \text{Cap}_{\text{intact}}$. Unlike the Pareto-based formulation, which explores trade-offs through the parameter α, the penalty method enforces a direct capacity target and therefore yields a unique repair pattern. The penalty parameter μ was selected empirically to ensure convergence to the target capacity.

Figure 8 illustrates the progressive evolution of predicted load capacity and deposited material with each iteration of the optimization process. A rapid initial increase in capacity is observed during the early iterations, as the optimizer identifies the most influential regions of the web and allocates material accordingly. During this phase, the violation of the capacity constraint $\big(L_{\text{goal}} - L(\mathbf{t})\big)$ is large, causing the penalty term in the objective function to dominate the gradient. As a result, material is preferentially added to regions exhibiting high sensitivity $\partial L/\partial t_i$.

As the target capacity is approached, the magnitude and direction of the gradient change significantly. The optimization gradually transitions from aggressively increasing local thickness to selectively refining the repair pattern by redistributing material toward regions with sustained structural influence. This transition is reflected in the curvature of the capacity and volume trajectories shown in Fig. 8. Once $|L_{\text{goal}} - L(\mathbf{t}_k)|$ becomes sufficiently small, the gradient of the penalized objective is dominated by the volume term, discouraging further deposition unless it yields a meaningful capacity increase.

In contrast with the Pareto front formulation, an adaptive step-size update strategy is employed for the penalty-based optimization. The step size η_k is reduced from its initial value of 0.20 to 0.04 and subsequently to 0.01 in response to oscillations observed during the early iterations (Fig. 8b). This reduction dampens the iterative updates and facilitates smooth convergence as both the design variables and the gradient norm decrease below the prescribed thresholds.

The final repaired pattern produced by the penalty method (Fig. 8a) deviates from the vertical reinforcement zones solutions observed for several Pareto-optimal cases (e.g., for $\alpha = 0.6$ or $\alpha = 0.7$ in Fig. 6d) and instead resembles the more broadly distributed reinforcement associated with the $\alpha = 0.5$ case. Notably, the total amount of deposited material for the penalty-based solution (154.19 cm^3) and for the $\alpha = 0.5$ Pareto solution (154.66 cm^3) are nearly identical, and both achieve comparable capacities of 914 kN and 915 kN,

respectively. A visual comparison further indicates that the penalty-based repair applies material to fewer grid elements overall, yielding a more compact pattern despite the similar total deposited volume. The close agreement between these independently obtained solutions provides additional confidence in the robustness and credibility of the proposed optimization framework.

5. Cold-Spray Deposition Architecture for Automated Repair Execution

While manual cold-spray repair has been demonstrated on in-service bridges in the Commonwealth of Massachusetts [38], the execution of optimization-derived, spatially programmed deposition patterns demands a mechanically guided and computationally coordinated deposition architecture. This section introduces a robotic cold-spray deposition architecture developed to bridge optimized repair design and physical execution. This deposition architecture could be applied to many other cases of structural steel repair, and the upstream optimization, choice of materials, and other suitable constraints could be adjusted accordingly.

5.1. Slicing and Path Planning

A dedicated post-processing script was developed to convert the optimized repair thickness field into an ordered, layer-wise deposition path suitable for automated execution. The script retrieves the Abaqus input file from the final optimization iteration, parses the nodal and elemental data, and identifies all repaired element sets within the web region. For each repaired element, the original shell thickness, added repair thickness, and nodal coordinates are extracted directly from the corresponding shell section definitions.

Deposition parameters, including nominal deposition (bead) width and layer height (t_{layer}), are specified based on the characteristics of the cold-spray equipment. To construct a continuous and kinematically feasible deposition sequence, element centroids are grouped according to their Z-coordinates, forming horizontal rows. When the bead width is smaller than the vertical spacing between adjacent element rows, linear interpolation is applied to enrich the coordinate set. Rows are processed sequentially from top to bottom or the opposite, with elements within each row ordered by increasing Y-coordinate . To reduce non-deposition travel and ensure continuous motion, every second row is traversed in reverse order (Fig. 9b-f), generating a serpentine (“snake-path”) trajectory.

Layer discretization is performed by subdividing the required deposited thickness using the user-defined layer height t_{layer}. For each element,

$$n_i = \left\lceil \frac{t_{\text{side},i}}{t_{\text{layer}}} \right\rceil$$

layers are required, where $t_{\text{side},i}$ denotes the total deposited thickness per side for element i. Each element is included in layers $L = 1, \ldots, n_i$. For each layer, the algorithm stores the ordered deposition coordinates, element indices, remaining thickness, and cumulative path length.

The resulting hierarchical data structure, containing all deposition layers and their corresponding paths, serves as direct input for generating machine-executable instructions for the automated deposition system.

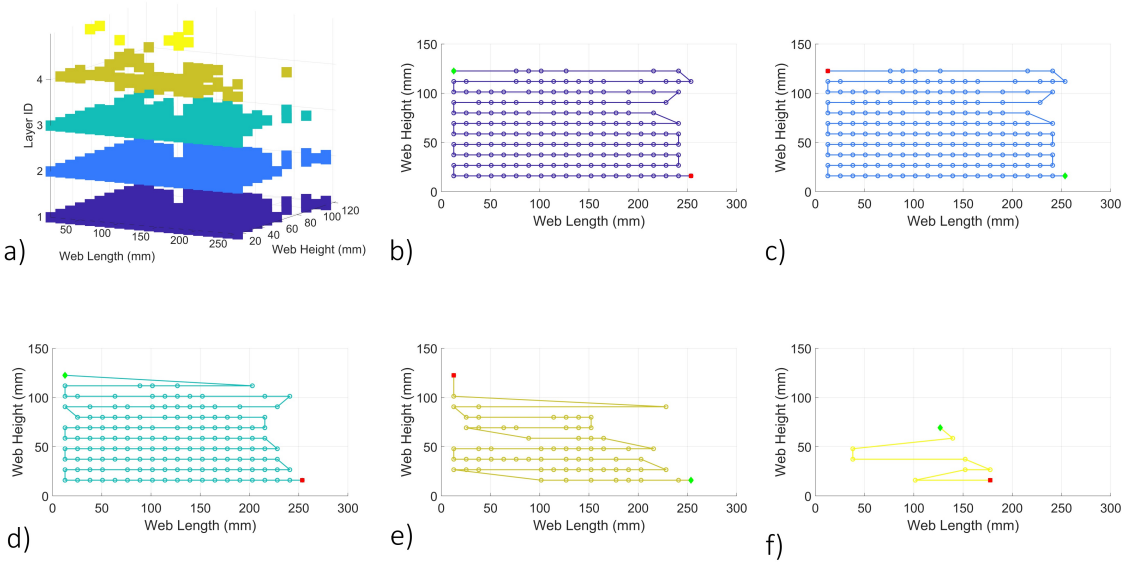

Figure 9: Conversion of optimized thickness fields into printing paths. (a) Indicative slicing of the optimal pattern obtained from the penalty method into five layers. (b–f) Illustration of the corresponding printing paths and generated machine-readable instructions. Markers along the paths indicate the locations of printable volumes, while the green and red colors denote the start and end points of each layer, respectively.

5.2. Functional Architecture and Design Constraints for Cold-Spray Repair

The design of a field-deployable cold-spray deposition system for bridge repair is governed by a combination of structural, geometric, and operational constraints that differ fundamentally from those encountered

in controlled manufacturing environments. Unlike conventional additive manufacturing systems, the deposition architecture must operate directly on existing steel girders, often in confined spaces, under variable environmental conditions, and with limited tolerance for misalignment or positional drift. These constraints strongly influence both the mechanical configuration of the system and the level of control required for reliable execution of optimized repair patterns.

A primary architectural requirement is the ability to establish and maintain accurate spatial registration between the deposition system and the corroded web region. Since optimized repair geometries are derived in a web-attached coordinate system, the deposition head must be positioned and actuated relative to the same reference frame, with consistent control of stand-off distance and nozzle orientation. This requirement places emphasis on rigid attachment to the girder and on minimizing compliance or vibration that could degrade positional accuracy during deposition.

Access constraints further shape the system architecture. Corrosion-driven section loss frequently initiates near the web–flange junction, necessitating unobstructed access to the full web height, including regions immediately adjacent to the bottom flange. The deposition system must therefore avoid geometric interference with the flange or surrounding structural components while still providing sufficient reach and maneuverability to execute spatially varying deposition paths.

Portability and deployability are equally critical considerations. To support practical use in bridge maintenance operations, the system must be sufficiently lightweight and compact to be transported and installed by a single operator, without reliance on cranes or specialized lifting equipment. Rapid attachment, detachment, and repositioning are essential for minimizing traffic disruption and enabling repairs at multiple locations along a structure. At the same time, the architecture must accommodate variability in girder geometry, particularly rolled I-shaped sections with depths representative of typical U.S. bridge construction.

Once installed, the system must provide a rigid and repeatable mechanical interface with the girder. The attachment mechanism must resist in-plane shear forces, out-of-plane bending moments, and dynamic loads induced by motion of the deposition head, ensuring that commanded trajectories remain consistent with the optimized repair maps. Any relative motion between the system and the substrate would directly translate into deposition errors and compromise the fidelity of the repair.

Finally, the architectural design must support robust operation in outdoor environments. Exposure to

moisture, temperature fluctuations, dust, and debris imposes additional demands on materials, actuation components, sensors, and electronics. The system must tolerate handling during transport and installation while maintaining reliable performance throughout the deposition process. Collectively, these constraints define the functional architecture of the proposed cold-spray repair system and motivate the mechanically simple, web-attached, and kinematically constrained design introduced in the following subsection.

5.3. Geometry and Mechanical Configuration

The proposed system, illustrated in Fig. 10a, consists of a rigid rectangular frame mounted directly onto the steel web. The frame dimensions are selected to accommodate beam depths between 50 cm and 91 cm, thereby covering the majority of rolled I-sections used in U.S. bridge construction. The two vertical members extend below the deposition mechanism, enabling unobstructed access to the web–flange junction where corrosion commonly initiates.

A cantilevered horizontal carriage rail is mounted on the frame and supports lateral translation of the deposition head. Positioned outboard of the web plane, this rail provides clearance from the magnetic attachment housings and ensures a consistent stand-off distance throughout the deposition process. This configuration minimizes mechanical complexity while maintaining access to the full height of the repair region.

The mechanical architecture provides three controlled degrees of freedom:

1. **Horizontal translation of the deposition head**, defining the primary raster direction for material placement;
2. **Vertical translation of the carriage rail**, enabling layer-wise advancement along the web height;
3. **In-plane stand-off adjustment**, achieved through controlled translation of the frame normal to the web plane to compensate for deposited material buildup.

This configuration supplies the minimum kinematic capability required for layer-by-layer additive deposition while avoiding the mass, complexity, and vibration sensitivity associated with multi-axis robotic arms. The frame is secured to the web using four magnetic attachment points. A preliminary sizing study accounting for operational loads and an assumed 0.1 mm protective coating on the web indicated that a

holding force of approximately 800 N per magnet is required. Suitable commercial magnets meeting these specifications are readily available in compact form factors.

During installation, a diagonal activation sequence is employed: the upper-left and lower-right magnets are engaged first to constrain rotation and in-plane translation, followed by activation of the remaining two magnets to fully lock the frame. Integrated bubble levels on the horizontal and vertical members allow rapid verification of alignment within the web-attached coordinate system, ensuring consistency between commanded deposition paths and finite element–derived repair maps.

5.4. Virtual System Development and Virtual Twin

Following the conceptual mechanical design, a digital representation of the cold spray architecture system was developed in MATLAB/Simulink using a model-based systems engineering approach. The resulting virtual twin reproduces the kinematic behavior of the moving components and enables simulation of the additive repair process under realistic geometric and operational constraints.

The Simulink environment includes an integrated interface allowing the user to select the girder type from a predefined library of commonly used beam sections (Fig. 10g). After girder selection, the user specifies the initial placement of the deposition head by defining global x and y offsets, analogous to registering the system at the upper-left corner of the repair region during field installation (Fig. 10a). Additional parameters allow adaptation of system characteristics based on geometric configuration and design requirements.

To simulate deposition, the relationship between deposition-head velocity, stand-off distance, and resulting bead geometry (width and height) is prescribed. Using these parameters in combination with the previously generated deposition paths, the virtual twin executes a full kinematic simulation of the repair process. The simulation animates the system motion in real time, visualizing each controlled degree of freedom as well as the activation sequence of the deposition process (Fig. 10b–f).

The developed digital environment is modular and supports conceptual, preliminary, and detailed system design. It enables rapid evaluation of alternative geometries, kinematic configurations, and control strategies. Furthermore, the modular structure allows future integration with a physical system: binary signals such as deposition activation, sensor feedback, and limit-switch states can be directly interfaced with Simulink blocks, providing a foundation for closed-loop control and real-time execution of automated additive repairs.

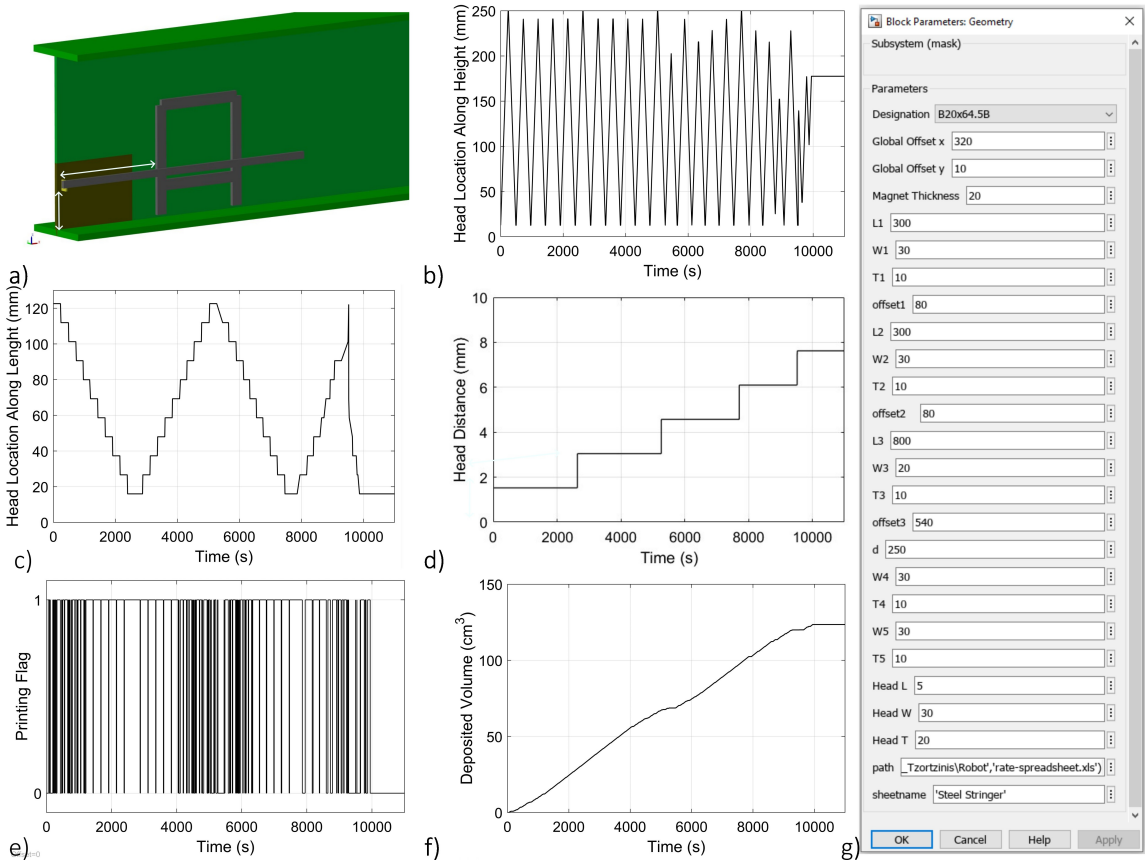

Figure 10: Robotic deposition architecture. (a) Conceptual design and virtual operation of a field-deployable robotic deposition architecture. (b–d) Simulated print-head motion along the three axes. (e) Printing-activation signal and f) evolution of deposited volume during printer operation. (g) The developed digital environment, which integrates beam geometries from a built-in library, offset definitions for registering the printer to a global coordinate system, and modular geometric characteristics for flexible configuration.

In addition, variations in positioning and actual deposition thickness can be fed back to the finite element simulation routine, along with actual post-repair scan data, to enable virtual and on-site qualification of the repair outcomes.

6. Discussion and Future Work

The methodology and results presented here represent a fundamental shift in how corrosion-induced material loss in steel bridge girders, and other structures, can be assessed and repaired. Conventional repair strategies rely heavily on manual surface preparation, including abrasive cleaning, removal of delaminated

steel, and application of protective coatings prior to the installation of welded or bolted reinforcement. These operations are labor-intensive, time-consuming, and often dominate the overall repair cost. In contrast, the cold-spray additive manufacturing process inherently cleans the substrate through high-velocity particle impact, which mechanically cleans and activates the steel surface during deposition. This characteristic suggests the feasibility of integrating a dedicated surface-conditioning or pre-cleaning pass directly within the automated deposition sequence, thereby reducing the need for extensive manual preparation. Given that surface cleaning is frequently among the most costly components of steel bridge repair operations, such integration has the potential to significantly improve both economic and operational efficiency.

A key contribution of this work is the high degree of automation achieved across the entire digital repair workflow. Each stage—laser-based corrosion mapping, structured thickness-field generation, finite element modeling, optimization, deposition-path planning, and virtual execution—is implemented using custom-developed algorithmic tools designed for seamless data exchange. By minimizing manual data handling and subjective interpretation, the workflow enables consistent and repeatable generation of repair strategies directly from measured deterioration states. This level of integration establishes a unified digital environment in which inspection data, structural analysis, and repair execution are coherently linked.

Future work will focus on experimentally validating and refining the material-deposition parameters that govern the physical execution of the optimized repairs. In particular, systematic testing is required to quantify the relationships among deposition-head velocity, stand-off distance, and resulting bead geometry. These experimentally derived relationships will provide the necessary inputs for the slicing algorithm and the virtual system model, enabling more accurate prediction of deposited geometries. In parallel, fabrication of the full-scale deposition system will allow laboratory validation of kinematics, attachment mechanisms, and deposition accuracy, followed by controlled field trials on representative steel girder segments.

The proposed workflow aligns closely with the principles of Industry 4.0 through its integration of cyber–physical systems and data-driven decision-making. The developed virtual twin provides a foundation for future coupling with the physical deposition system, enabling simulation, optimization, and execution within a unified control architecture. Through structured data exchange among sensing, computation, and actuation modules, the framework supports informed decisions regarding repair extent, deposition strategy, and expected structural performance. Such tightly integrated systems are central to emerging paradigms in

automated infrastructure maintenance.

Beyond the specific application to steel bridge girders, the methodology developed in this study has broader applicability to other corrosion-prone infrastructure systems. Maritime and offshore structures, in particular, experience localized material loss under constrained access conditions and harsh environments, making automated surface-conditioning and additive repair technologies especially attractive. By adapting the scanning strategy, geometric parameterization, and deposition hardware to different structural forms, the same detection, quantification, optimization, and repair pipeline could enable safer, more precise, and more efficient maintenance across multiple industrial sectors.

7. Conclusions

The main contributions and conclusions are summarized as follows:

- A structured grid-based representation of corrosion was shown to provide accurate prediction of residual beam structural capacity while significantly reducing model complexity and computational cost, enabling iterative optimization analyses.
- A gradient-based optimization framework was developed to identify material-efficient reinforcement patterns. Pareto-front solutions revealed distinct strengthening strategies that balance added material volume and recovered load-carrying capacity.
- A penalty-based optimization formulation successfully achieved prescribed target capacities relevant to bridge load rating, producing repair patterns consistent with Pareto-optimal solutions and demonstrating the robustness of the computational approach.
- A fully integrated digital workflow was established, spanning laser scanning, corrosion mapping, finite element modeling, optimization, deposition-path planning, and virtual execution, with minimal reliance on manual intervention.
- A conceptual cold spray architecture and its virtual twin were developed to translate optimized deposition fields into machine-executable repair actions under realistic field constraints.

- The overall methodology aligns with Industry 4.0 principles through the coupling of cyber–physical systems, digital twins, and data-driven decision-making for automated infrastructure maintenance.

While demonstrated for steel bridge girders, the proposed framework is readily adaptable to other corrosion-prone infrastructure systems, including maritime and offshore structures, offering an actionable pathway toward precise, automated, resource-efficient, and data-informed repair technologies.

8. Data Statement

Selected data are available from the corresponding author upon reasonable request.

9. Author Contributions

Georgios Tzortzinis: Conceptualization, Formal analysis, Investigation, Methodology, Visualization, Software, Writing – original draft. Kaushik Abhyankar: Software, Methodology. Bruno Guilherme Christoff: Methodology. Brian Schagen: Investigation. A. John Hart: Writing – review and editing. Simos Gerasimidis: Writing – review and editing, Investigation. Maik Gude: Writing – review and editing.

References

[1] G. Tzortzinis, B. T. Knickle, A. Bardow, S. F. Breña, S. Gerasimidis, Strength evaluation of deteriorated girder ends. I: Experimental study on naturally corroded I-beams, Thin-Walled Struct. 159 (2021) 107220. doi:10.1016/j.tws.2020.107220.

[2] G. Tzortzinis, B. T. Knickle, A. Bardow, S. F. Breña, S. Gerasimidis, Strength evaluation of deteriorated girder ends. II: Numerical study on corroded I-beams, Thin-Walled Structures 159 (2021) 107216. doi:10.1016/j.tws.2020.107216.

[3] G. Tzortzinis, S. F. Breña, S. Gerasimidis, Experimental testing, computational analysis and analytical formulation for the remaining capacity assessment of bridge plate girders with naturally corroded ends, Engineering Structures (2022). doi:10.1016/j.engstruct.2021.113488.

[4] Y. Wang, S. Xu, A. Li, Flexural performance evaluation of corroded steel beams based on 3d corrosion morphology, Structure and Infrastructure Engineering 16 (11) (2020) 1562–1577. doi:10.1080/15732479.2020.1713169.

[5] J.-H. Ahn, S. Kainuma, F. Yasuo, I. Takehiro, Repair method and residual bearing strength evaluation of a locally corroded plate girder at support, Engineering Failure Analysis 33 (2013) 398–418. doi:10.1016/j.engfailanal.2013.06.015.

[6] B. Wu, J.-L. Cao, L. Kang, End patch loading behavior and strengthening of locally corroded steel i-beams, Journal of Constructional Steel Research 148 (2018) 371–382. doi:10.1016/j.jcsr.2018.05.029.

[7] T. Zhang, A. E. Zaghi, Estimation of the residual bearing strength of corroded bridge girders using 3d scan data, Thin-Walled Structures 188 (2023) 110798. doi:10.1016/j.tws.2023.110798.

[8] A. Tarasova, D. Kanakamedala, A. H. Varma, J. Seo, R. J. Connor, Assessment of innovative repair methods for corroded steel girder bridges using the house of quality matrix, Transportation Research Record 2678 (2) (2024) 563–573.

[9] Z. Li, Z. Fu, B. Ji, L. Wan, Y. Yao, Reinforcement effect of corroded end in steel girder with multi-transverse web stiffeners, Journal of Constructional Steel Research 216 (2024) 108577. doi:10.1016/j.jcsr.2024.108577.

[10] T. Miyashita, M. Nagai, D. Wakabayashi, Y. Hidekuma, A. Kobayashi, Y. Okuyama, N. Koide, W. Horimoto, Repair method for corroded steel girder ends using cfrp sheet, in: IABSE-JSCE Joint Conference on Advances in Bridge Engineering-III, 2015.

[11] H. Ogami, K. Fujii, T. Yamada, H. Iwashaki, Renovation of corroded girder end in plate girder bridge with resin and rebars, in: Implementing Innovative Ideas in Structural Engineering and Project Management, 2015.

[12] K. M. Zmetra, K. F. McMullen, A. E. Zaghi, K. Wille, Experimental study of uhpc repair for corrosion-damaged steel girder ends, Journal of Bridge Engineering 22 (8) (2017) 04017037. doi:10.1061/(ASCE)BE.1943-5592.0001067.

[13] D. Kruszewski, K. Wille, A. E. Zaghi, Design considerations for headed shear studs embedded in ultra-high performance concrete as part of a novel bridge repair method, Journal of Constructional Steel Research 149 (2018) 180–194. doi:10.1016/j.jcsr.2018.07.015.

[14] D. Kruszewski, K. Wille, A. E. Zaghi, Push-out behavior of headed shear studs welded on thin plates and embedded in uhpc, Engineering Structures 173 (2018) 429–441. doi:10.1016/j.engstruct.2018.07.013.

[15] D. Kruszewski, A. E. Zaghi, K. Wille, Durability evaluation of headed shear studs embedded in ultrahigh-performance concrete via electrochemical corrosion, Journal of Bridge Engineering 24 (5) (2019) 04019038. doi:10.1061/(ASCE)BE.1943-5592.0001401.

[16] B. Lassy, A. Hain, A. E. Zaghi, Z. M. Kanyo, B. K. Chuong, A. Cardinali, Rehabilitation of corroded steel bridge girder ends using partial-height ultra-high-performance concrete encasement, Transportation Research Record 2678 (6) (2024) 178–195. doi:10.1177/03611981231194629.

[17] S. W. Williams, F. Martina, A. C. Addison, J. Ding, G. Pardal, P. Colegrove, Wire + arc additive manufacturing, Materials Science and Technology 32 (7) (2016) 641–647. doi:10.1179/1743284715Y.0000000073.

[18] C. V. Haden, G. Zeng, F. Carter, C. Ruhl, B. Krick, D. G. Harlow, Wire and arc additive manufacturing of steel: A review, Additive Manufacturing 23 (2018) 595–607. doi:10.1016/j.addma.2018.08.007.

[19] J. Zhang, Y. Li, Y. Chen, Mechanical performance and microstructure of wire arc additively manufactured structural steel, Journal of Constructional Steel Research 170 (2020) 106090. doi:10.1016/j.jcsr.2020.106090.

[20] H. Assadi, F. Gärtner, T. Stoltenhoff, H. Kreye, Bonding mechanism in cold gas spraying, Acta Materialia 51 (15) (2003) 4379–4394. doi:10.1016/S1359-6454(03)00274-X.

[21] F. Gärtner, T. Stoltenhoff, T. Schmidt, H. Kreye, The cold spray process and its potential for industrial applications, Journal of Thermal Spray Technology 15 (2006) 223–232. doi:10.1361/105996306X108110.

[22] T. Schmidt, F. Gärtner, H. Assadi, H. Kreye, Development of a generalized parameter window for cold spray deposition, Acta Materialia 54 (2006) 729–742. doi:10.1016/j.actamat.2005.10.005.

[23] V. K. Champagne, The cold spray materials deposition process, Woodhead Publishing (2007).

[24] J. Villafuerte, Modern cold spray: materials, process, and applications, Springer (2018).

[25] K. Kang, H. J. Kim, C. Lee, Repair of damaged steel components by cold spray deposition, Journal of Thermal Spray Technology 26 (2017) 117–130.

[26] R. J. Ross, B. K. Brashaw, S. J. Anderson, Use of laser scanning technology to obtain as-built records of historic covered bridges, USDA Forest Service, Forest Products Laboratory, Report Paper, FPL-RP-669, 2012; 21 p. 669 (2012) 1–21.

[27] I. Lubowiecka, J. Armesto, P. Arias, H. Lorenzo, Historic bridge modelling using laser scanning, ground penetrating radar and finite element methods in the context of structural dynamics, Engineering Structures 31 (11) (2009) 2667–2676. doi:10.1016/j.engstruct.2009.06.018.

[28] M. Minehane, R. O'Donovan, K. Ruane, B. O'Keeffe, The use of 3d laser scanning technology for bridge inspection and assessment, Structural Health Monitoring (SHM) 13 (2014) 14.

[29] C. Popescu, B. Täljsten, T. Blanksvärd, L. Elfgren, 3d reconstruction of existing concrete bridges using optical methods, Structure and Infrastructure Engineering 15 (7) (2019) 912–924. doi:10.1080/15732479.2019.1594315.

[30] L. Truong-Hong, H. Falter, D. Lennon, D. F. Laefer, Framework for bridge inspection with laser scanning, in: in Proceedings of the EASEC-14 Structural Engineering and Construction, Ho Chi Minh City, Vietnam, 2016.

[31] S. K. P. Kushwaha, S. Raghavendra, H. Pande, S. Agrawal, Analysis and integration of surface and subsurface information of different bridges, Journal of the Indian Society of Remote Sensing 48 (2) (2020) 315–331.

[32] H.-K. Shen, P.-H. Chen, L.-M. Chang, Automated steel bridge coating rust defect recognition method based on color and texture feature, Automation in Construction 31 (2013) 338–356. doi:10.1016/j.autcon.2012.11.003.

[33] G. Tzortzinis, A. Filippatos, J. Wittig, M. Gude, A. Provost, A. C. S. Gerasimidis, Structural integrity of aging steel bridges by 3d laser scanning and convolutional neural networks, Communications Engineering 3 (2024) 2731–3395. doi:10.1038/s44172-024-00255-8.

[34] G. Tzortzinis, C. Ai, S. F. Breña, S. Gerasimidis, Using 3d laser scanning for estimating the capacity of corroded steel bridge girders: Experiments, computations and analytical solutions, Engineering Structures 265 (2022) 114407. doi:10.1016/j.engstruct.2022.114407.

[35] Riegl, Riegl VZ-2000 brochure (2020).

[36] MassDOT, Draft LRFD Bridge Manual Part I, Boston, MA (2020).

[37] G. Tzortzinis, S. Gerasimidis, S. F. Breña, B. Knickle, Development of load rating procedures for deteriorated steel beam ends, Tech. Report 19-008, MassDOT (2019).

[38] A. Wilson, "Cold spray" 3D printing technique proves effective for on-site bridge repair, https://news.mit.edu/2025/cold-spray-3d-printing-technique-effective-bridge-repair-0620, accessed: November 23, 2025 (Jun. 2025).